Winds near the Surface of Waves: Observations and Modeling

ALEXANDER V. BABANIN

University of Melbourne, Melbourne, Victoria, Australia

JASON MCCONOCHIE

Shell Global Solutions International B.V., The Hague, Netherlands

DMITRY CHALIKOV

University of Melbourne, Melbourne, Victoria, Australia, and P. P. Shirshov Institute of Oceanology, St. Petersburg, Russia

(Manuscript received 20 January 2017, in final form 6 March 2018)

ABSTRACT

The concept of a constant-flux layer is usually employed for vertical profiling of the wind measured at some elevation near the ocean surface. The surface waves, however, modify the balance of turbulent stresses very near the surface, and therefore such extrapolations can introduce significant biases. This is particularly true for buoy measurements in extreme conditions, when the anemometer mast is within the wave boundary layer (WBL) or even below the wave crests. In this paper, field data and a WBL model are used to investigate such biases. It is shown that near the surface the turbulent stresses are less than those obtained by extrapolation using the logarithmic-layer assumption, and the mean wind speeds very near the surface, based on Lake George field observations, are up to 5% larger. The behavior is then simulated by means of a WBL model coupled with nonlinear waves, which confirmed the observations and revealed further details of complex behaviors at the wind-wave boundary layer.

1. Introduction

Modeling and measurements of the winds over the ocean surface are important in engineering, geophysics, remote sensing, and other metocean applications. The wind-wave/current interactions, or more generally air–sea energy and momentum exchanges, happen directly at the ocean interface, but measuring wind speeds and momentum right at the surface is difficult in field conditions, particularly at heavy seas which are usually of the main interest. Therefore, the 10-m elevation is routinely accepted as a standard height for representative wind speed U_{10}, which nowadays is also often offered as an output of atmospheric meteorological models and is typically employed as input for wave-forecast and other air–sea interaction models.

There are, however, problems with this standard height. Measurements at exactly 10 m are hardly ever available in the ocean, and hence extrapolations of available measurements (up or down) are involved. Pierson and Moskowitz (1964), for example, used wind measurements at 19.5-m height to produce the benchmark nondimensional concept of fully developed sea state, and for some years it became a standard height. Young et al. (2005), in a dedicated field experiment, did set their top anemometer at 10 m above the mean water level of Lake George; however, as the lake was drying out, the water level was changing and this elevation was drifting, so corrections to the measured wind were needed to bring it to the 10-m standard. Also, significant oscillations of the mean level were observed as a result of seiches. Babanin et al. (2016) described a field observation site 120 km off the northwest coast of Australia, in the path of tropical cyclones, where sonic anemometers are deployed below the flair bridge at 9 and 15 m above the mean sea level. Even in such offshore conditions, the water level (and hence the elevation of the anemometer above the water) is subject to tidal variations, and there is a possibility that the lower anemometer can be swept by hurricane waves.

Corresponding author: Alexander Babanin, a.babanin@unimelb.edu.au

DOI: 10.1175/JPO-D-17-0009.1

More routine are buoy measurements of wind where an anemometer is placed on a mast mounted on a discus buoy. These are moving platforms, which fact further complicates the interpretation of mean wind speeds and fluxes measured. Besides, the buoy anemometer masts are typically less than 10 m high. When waves are big, such masts can be below wave crests intermittently, and when the waves are very big, even the reference 10-m height above the mean water level can be below the surface occasionally.

Very early it was noticed that "measurements from buoys and fixed masts show marked differences." The quote is from Pond (1968, p. 507), who in an analytical paper demonstrated that reliable measurements of wind speed and stress from a buoy require keeping its tilt very small—something very difficult at sea, particularly for strap-down buoys. Skey et al. (1998) and Taylor et al. (2002) presented results of the field observations of the winds from a standard Navy Oceanographic Meteorological Automatic Device (NOMAD) weather buoy of Environment Canada (SWS-1 and SWS-2 campaigns, respectively), including some very large waves with significant wave height up to 9.4 m. They found the effect of pitch-and-roll motions small and the difference between scalar and vector winds to be only 1%–4%. The effect of wind sheltering while the buoys are in the troughs of large waves, however, was essential, leading to reduction of the measured wind speed, which was increasing as a function of the wave height. Howden et al. (2008) measured winds from a 3-m discus buoy within Hurricane Katrina. A mechanical anemometer (R. M. Young 5106) failed during the event, and a two-axis sonic Gill anemometer survived. By comparing the two independent wind records when both were operational, the authors reported that the buoy's pitch-and-roll motions impose deviations that require corrections for anemometer readings for winds oblique to their horizontal plane.

For the extrapolations, the semilogarithmic profile of wind speed is usually assumed in the atmospheric boundary layer, by analogy with the fluid flow over solid wall (e.g., Landau and Lifshitz 1987). In the geophysical system, this logarithmic profile, given by

$$U(z) = \frac{u_*}{K} \ln \frac{z}{z_0}, \tag{1}$$

is the solution of the horizontal-momentum equations for the near-surface boundary sublayer dominated by friction forces, both viscous and turbulent (e.g., Komen et al. 1994):

$$\partial \tau / \partial z = 0. \tag{2}$$

Here, U is the wind speed at height z above the mean undisturbed water level, $\kappa = 0.41$ is the dimensionless von Kármán constant, z_0 is the surface-roughness length scale [note that this scale is orders of magnitude smaller than the wave height (e.g., Kitaigorodskii 1970)]. The friction velocity u_* has a dimension of speed, but is not a speed in the physical space. By definition, it is the square root of the normalized vertical flux of the horizontal momentum, or turbulent wind stress τ:

$$\tau = \rho_a u_*^2 = \rho_a C_d U_{10}^2, \tag{3}$$

where C_d is the drag coefficient.

In the boundary sublayer described by (2), the wind stress τ, apparently, does not depend on height z (hence, the constant-flux layer). Since τ is the turbulent stress, friction velocity u_* can be obtained both from the wind profiles in (1) and measured directly:

$$u_*^2 = -\overline{U'w'}, \tag{4}$$

where U' and w' are fluctuations of the horizontal and vertical velocities, correspondingly, and the overbar signifies ensemble average.

Comparisons of friction velocity obtained from measurements of the velocity profile in (1) and the turbulence stresses in (4) have been conducted before and show good agreement, except for low wind speeds ($U_{10} < 4\,\mathrm{m\,s^{-1}}$) where the condition of the uniform constant-flux layer is most likely not satisfied (e.g., Babanin and Makin 2008). At light winds, this is, among other possible reasons, due to wind gustiness, which causes the wind to vary widely in both magnitude and direction with respect to the mean [note that at such winds the constant-flux layer, if it exists, can be below the standard-measurement height of 10 m (Komen et al. 1994)]. Generally, most common reasons for deviations from or even violation of the constant-flux assumption are nonstationarity and nonhomogeneity of wind fields, which in fact are more common than stationarity and homogeneity, whether because of the transient unsteady nature of meteorological phenomena or simply owing to large-scale vorticity/turbulence. Overall, therefore, geophysical conditions meet the analogy with the flow over solid wall only approximately, and in a general case this analogy requires empirical modifications [e.g., adjustments of the logarithmic profile in (1)] to account for deviations caused by the atmospheric stratification (Monin and Obukhov 1954).

The big difference with the solid wall, however, is that the surface roughness is due to wind-generated waves, which are mobile and grow, and as they grow, they are changing the very wind that is generating them (e.g., Kitaigorodskii 1970; Komen et al. 1994; Babanin and Makin 2008). Most of the energy lost from the wind over

the ocean is not dissipated but is passed on to waves, turbulence, and currents. At moderate and strong winds, the momentum lost by winds largely goes to the waves, whereas at light winds to the currents (e.g., Kudryavtsev et al. 2001; Chalikov and Rainchik 2011, hereinafter CR11). These are two absolutely different physical regimes as far as air–sea momentum exchange is concerned: in the first case, wind passes the momentum by means of pressure forces (form drag) and in the second by means of tangential stresses (skin drag). Thus, at strong winds the skin drag in the budget of air–sea interactions is unessential, which is a vast difference with the wall-flow dynamics. Furthermore, the waves redistribute the energy within the wave spectrum by means of nonlinear interactions (Hasselmann 1962), part of which can go to waves moving faster than the wind and be returned back to the wind (e.g., Donelan 1999; Donelan et al. 2012). The wavy surface is never homogeneous; waves form groups and break sporadically thus causing localized enhancements of the sea drag (e.g., Babanin et al. 2007; Babanin 2009) and energy passed back to the atmospheric turbulence (Iafrati et al. 2013, 2014).

Importantly, the waves create their own wave boundary layer (WBL) in the atmosphere (e.g., Chalikov and Belevich 1993; CR11), superposed on the near-surface boundary sublayer discussed above. Within such a sub-sublayer, dynamics is very different from the constant-flux ideas. Wave-induced fluxes are not constant; they oscillate in magnitude and alter the sign over a wave period. Wave-coherent pressure/velocity fluctuations are produced in the air. The magnitude of such fluctuations depends on a variety of characteristics of wind-wave exchanges, and their phase is shifted with respect to the wave that produced them (e.g., Donelan et al. 2006). These pulsations decay rapidly away from the surface, but down close to the surface, the wave-induced flux dominates and ultimately replaces the flux owing to random turbulence (e.g., Komen et al. 1994; Kudryavtsev et al. 2001; CR11). The vertical extent of the WBL depends on wavelength of dominant waves, which for the wind-generated waves is from tens of meters to hundreds of meters, but a noticeable intensity of wave-induced/coherent fluctuations is only expected at the scale of wave height, hence very near the surface (CR11).

Within the WBL, deviations from the expressions and predictions in (1)–(4) can be expected. Babanin and McConochie (2013) discussed these deviations based on field observation in Lake George (Australia), and the experimental part of the present paper largely follows this discussion. Hara and Sullivan (2015) offered analytical theory and LES simulations that demonstrated such differences for the WBL in extreme wind-forcing conditions.

These deviations have practical significance for engineering, meteorological, and geophysical applications. First of all, as a result, extrapolations based on the assumed logarithmic profile may not be accurate or even correct, particularly as the ''standard'' 10-m wind-measurement height may be in or out of the WBL, depending on wave conditions. This would impact estimates of the mean wind speed. Wave-induced disruptions of the constant-flux layer bring about uncertainty and ambiguity about the turbulent stress, momentum flux, and drag coefficient in (2)–(4).

Such uncertainties are particularly relevant with respect to buoy measurements of the wind speed. As discussed above, the buoy-located anemometers move and are subject to tilting, and in an ideal scenario they are kept at a constant height above an instantaneous water surface, rather than above the mean water level like the standard representative 10-m wind reference. In extreme wave conditions, however, because the measurements are close to the surface and sometimes even below wave crests, they are likely to be within the WBL and therefore are moving through the oscillatory vertical fluxes of horizontal momentum in a complicated manner.

In this paper, measurements of the mean wind speeds and momentum fluxes are conducted in what is meant to be a constant-flux layer, including very close to the wavy water surface. The latter is performed by a wave follower in both the following and stationary (i.e., fixed above the mean level) modes. The follower is not floating; it is deployed on a bridge above the water surface, senses the instantaneous surface elevation, and moves the arm with probes up and down, correspondingly. In the second part of the paper, the coupled WBL model of CR11 is used in the analysis of the measured properties of wave boundary layer at winds ranging from light to strong and for sea states from young to old waves.

There are two important practical questions associated with this study: How do extrapolations of measurements of winds and turbulent stresses very near the surface, up to the standard height above the mean water level, compare with the actual stationary measurements at 10 m, and how do the measurements in the surface-following mode and in the stationary (with respect to the mean water level) mode agree with each other within the WBL? The latter comparison, clearly, has to be above the height of wave crests; otherwise the probe would be submerged for some part of the time.

This is an experimental paper, and section 2 describes the measurements and the methods and presents the experimental results. Section 3 provides results of the

WBL modeling in the context of the experimental discussion in order to understand, explain, and extend the conclusions to a broader range of sea-state conditions. These are followed by a summary in section 4.

2. Observations

The Lake George finite-depth field experiment is well documented, and we refer to Young et al. (2005) for a summary and to Donelan et al. (2005) for details of the wave-following system and measurements. All measurements were synchronized, with most of them sampled at a 25-Hz rate. Many measurements, particularly those in the atmospheric boundary layer, were intentionally redundant in order to provide momentum flux estimates by separate independent means (Babanin et al. 2005; Babanin and Makin 2008; Babanin and McConochie 2013).

The wind profile was obtained by means of the anemometer mast with six cup anemometers logarithmically spaced from 10-m height down to 0.5 m above the mean sea level. The wind probes were Aanderaa Instruments Wind Speed Sensors 2740 and provided 1-min average wind speeds and gusts. Accuracy of the wind speed measurements is ±2% or 0.2 m s^{-1}, whichever is greater. Thus, the cup anemometers allowed direct estimates of wind speeds at the six heights and estimates of u_* from (1).

For redundancy in the wind speed measurements and momentum-flux estimates, a Gill Instruments Ultrasonic Anemometer was also deployed on the mast, with the sensing volume fixed 4.6 m above the varying mean water level, with sampling at 21 Hz. In Babanin and Makin (2008), 33 wind records taken in different conditions simultaneously by the anemometer mast and by the fixed sonic anemometer were compared. Overall matching in terms of absolute values of u_* obtained from the profile [(1)] and from the flux [(4)] was good, with a correlation coefficient of 95% and sampling standard deviation of 0.06 m s^{-1}. Horizontal velocity U used for the turbulent stress [(4)] was the length of vector sum of the downwind and crosswind components.

During a dedicated phase of the Lake George experiment, the wave follower developed at the University of Miami was deployed (Donelan et al. 2005). It was the primary tool to enable direct measurements of the wind energy input because it allowed us to conduct relevant environmental readings very near the surface, and hence will be the main source of information for the present paper. The follower was installed on a special platform that could be rotated and thus allowed us to align the sensors into the wind and wave directions. The signal from a resistance probe, consisting of a loop with vertical wires separated by 10 cm, was used to determine the instantaneous position of the surface midway between the vertical arms; it is in the same (x, z) position as the ports of the Elliott pressure disk (Elliott 1972), which was constrained to move vertically by the wave follower. This was the signal that the wave follower was designed to follow. When in operation, the follower's arm would carry the Elliott pressure disk at the bottom as close to the surface as possible (within a few centimeters), a hot wire set at 10 cm directly above, and a Pitot tube at the top.

The wave-follower instrumentation sampling frequency was 50 Hz, twice the rate of the other instrumentation. To synchronize the two independent measurement systems, a sawtooth signal was generated and recorded by both the wave follower and the main logging computer. When operating in the following mode, the wave follower and the water surface were videotaped, also at the rate of 25 frames per second, and synchronized with the other measurements.

In this paper, hot-wire records from the wave follower are used in addition to the anemometer-mast and sonic-anemometer wind and flux measurements. Two hot-wire probes were located on the wave follower: one on the moving arm, 10 cm above the Elliott probe as mentioned above, and a pair stationary with respect to the mean water level 1.5–1.7 m above the water surface (depending on the varying water depth). The hot-wire records enabled us to obtain variations of the local stresses in (4) very close to the surface in conjunction with other wind and wave properties and to estimate mean momentum fluxes.

Wave measurements were conducted by an array of eight capacitance wave probes manufactured by Richard Brancker Research, Ltd., Canada. The sensing probes were Teflon-coated wires, 1 m long and 1 mm thick. Manufacturer specifications guaranteed 0.2% linearity and 0.4% accuracy, as well as a 2-ms time response. For the Lake George measurements a Brancker model WG-30 system was used, which was designed to operate in a master/slave time-sequenced format so that two or more probes could be positioned together (less than 100 cm apart) and still avoid interference. Since the probes were positioned much closer than 100 cm, thorough laboratory tests were performed with the prepared array prior to its field deployment in order to verify that interference effects were negligible. In addition, accurate calibrations were done at the laboratory, and facilities for quick calibration in the field were set up at the measurement platform. Calibrations were performed frequently, and the calibration characteristics of the gauges proved remarkably stable during the 3-yr-long experiment.

Details of the experiments (distances from the surface for the mobile hot wires and the water depths at the time

of a measurement) and air–sea conditions, as measured by the anemometer mast, the sonic anemometer, and the hot wires, as well as wave characteristics [peak frequency and significant wave height (H_s)] are given in Table 1 [see also Donelan et al. (2006) for more details]. Here we will mention that the distances of the bottom hot-wire from the water surface were from 12 to 48 cm, ratios of the bottom hot-wire elevation to H_s were from 0.7 to 7, and ratios of this elevation to wavelength from 0.04 to 0.23. As described above, the bottom hot wire was located at the moving arm of the follower, and it was operated in two modes: following and fixed. In the case of the latter, the arm was not moving and then all the sensors (note that the Elliott disk is 10 cm below the hot wire) were located above the wave crests as they have to stay dry in order to operate.

Wave-induced fluxes in the WBL should depend on both wavelength and height of the waves that produced them (see also Donelan et al. 2006). Scatter of the data, however, was large and it proved not possible to stratify the measurements in these terms. Here, we separated the direct flux measurement by sensors: those by the sonic anemometer, by the top hot wire, and by the bottom hot wire. The top hot wire was always stationary, and for cross-references with the bottom wire the following-mode records are designated with asterisks in Figs. 1 and 2 and the fixed-mode records with circles, for both hot wires.

In Fig. 1, stresses measured by the top hot wire (fixed) and bottom hot wire are compared with those measured by the sonic anemometer well above the surface (~4.6 m). Blue signifies the bottom hot wire and red signifies the top.

Friction velocity u_* obtained from the hot wires is compared with the sonic u_* in the left panel of Fig. 1. The straight line denotes a 1:1 ratio. As expected, the hot-wire measurements are below the line (see section 3), but the difference between the top hot wire and bottom hot wire is quite dramatic. Note that zero-reading values have to be disregarded—these are points where either the hot wire or the sonic anemometer did not have a reading but the data points are kept here for cross-reference reasons within this and other papers based on Lake George measurements.

The difference is further quantified in the right panel of Fig. 1 where ratio of hot-wire u_* to the sonic u_* is plotted versus wind speed U_{10} from the anemometer mast. For both groups, the ratio is rather constant. The mean ratio of the top u_* to the sonic u_* is 0.86, and for the bottom u_* it is 0.32 (i.e., 2.7 times smaller, which is 7.3 times for the fluxes). This difference cannot be attributed to the fact that the bottom probe was moving and following the surface. On average, there is no difference between the readings taken in the following and fixed modes of data sampling. Therefore, the remarkable reduction of the fluxes near the surface, measured by the top hot wire and bottom hot wire just over 1 m apart, should be linked to the properties of the wave boundary layer superposed on the constant-flux layer as discussed in section 1 above.

In the constant-flux layer, smaller turbulent stresses would signify a reduction of surface resistance and increase of the mean wind speed. In the WBL, however, this is not so obvious as the momentum is now taken from the wind through the air pressure/wave-slope term $\overline{p(\partial\eta/\partial x)}$, where pressure oscillations are wave induced and not random on average as represented by the overbar. Exact balance of the turbulent momentum flux τ and the abovementioned wave-induced momentum flux is not known analytically and has to be modeled numerically by means of, for example, a coupled three-dimensional model of nonlinear waves and the WBL as in CR11 (see section 3 below).

TABLE 1. Summary of the records used in the present study; the top records are in the fixed mode, and the bottom records in the following mode. The first four columns are different estimates of the friction velocity ($m\,s^{-1}$): u_{*S} is by the sonic anemometer, u_{*b} and u_{*t} are by the bottom and top hot wires, respectively, and u_{*p} is obtained from the anemometer-mast wind profile. The next three columns are values of mean wind speeds ($m\,s^{-1}$): U_{10} is the standard 10-m wind speed obtained from the anemometer-mast wind profile, and U_b and U_t are from the bottom and top hot wires, respectively. The h (mm) is the elevation of the bottom hot wire above the water surface (mean surface in case of the fixed mode and instantaneous surface in case of the following mode), and d (mm) is the water depth at the time of the measurements. The f_p is wave peak frequency (Hz), and H_s is significant wave height (m).

u_{*S}	u_{*b}	u_{*t}	u_{*p}	U_{10}	U_b	U_t	h	d	f_p	H_s
Fixed										
0.38	0.21	0.27	—	9.2	7.0	7.5	470	263	0.67	0.065
0.34	0.04	0.35	—	8.2	5.6	6.5	354	279	0.62	0.055
0.35	0.04	0.30	0.31	8.9	5.3	5.9	402	231	0.64	0.092
0.40	0.14	0.32	0.31	8.9	5.2	6.1	295	238	0.79	0.100
0.34	0.11	0.34	0.32	9.0	5.0	6.0	267	216	0.86	0.106
0.35	0.08	0.31	0.30	8.6	5.2	6.2	243	240	0.66	0.087
0.33	0.27	0.32	0.27	8.5	6.0	6.5	484	249	0.67	0.068
Following										
—	0.18	—	0.18	6.6	4.2	—	126	308	—	—
0.57	0.26	—	0.44	11.9	5.9	—	121	319	0.54	0.156
0.39	0.16	0.30	0.26	8.1	5.7	6.6	249	329	0.76	0.076
0.54	0.12	0.45	0.36	10.6	7.9	8.7	356	315	0.57	0.078
0.30	0.13	0.30	0.22	7.1	4.8	5.6	291	270	—	—
0.37	0.10	0.31	—	7.3	4.9	5.8	302	276	0.60	0.065
0.35	0.07	0.31	0.23	7.4	4.6	5.3	391	287	0.81	0.065
0.32	0.08	0.28	0.23	7.3	4.3	5.1	294	254	0.86	0.074
0.40	0.11	0.30	0.36	9.5	5.3	6.1	388	272	0.83	0.070
0.31	0.04	0.20	0.20	6.4	3.4	4.3	149	259	—	—
0.22	0.05	0.20	0.19	6.4	3.2	4.2	134	254	—	—

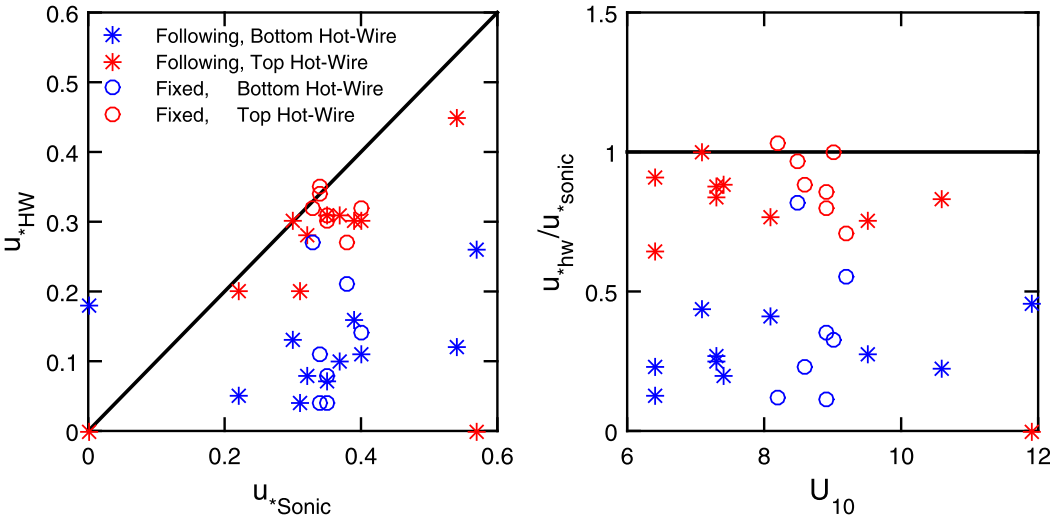

FIG. 1. (left) The u_* measured by hot wires near the surface vs u_* measured by the sonic anemometer at 4.6-m height. (right) Ratio of the hot-wire and sonic-anemometer u_* vs U_{10}. In both panels, asterisks indicate the following mode and circles the fixed mode, and blue indicates the bottom hot wire and red the top hot wire. Note that the top hot wire is always stationary.

In Fig. 2, implications of the observed reduction of the turbulent flux for the wind profile are shown. The mean wind speed U_b at the bottom hot-wire altitude z_b is predicted by assuming the logarithmic law in (1) and using measurements of the mean wind speed U_t and friction velocity u_{*t} by the top hot wire z_t (vertical scale in Fig. 2):

$$U_b = U_t + \frac{u_{*t}}{K} \ln \frac{z_b}{z_t}.$$

This predicted speed is compared with the actual measurements of the mean wind speed by the bottom hot wire (horizontal scale). The straight line is 1:1 ratio.

All the data points, both for the following and fixed modes, are below the line. Therefore, the actual wind speed very near the surface is always larger than the extrapolation. The mean ratio of the two is 1.05; that is, the systematic difference is 5% in this set of measurements.

3. Modeling

Experimental results of section 2 can be explained within the framework of WBL theory (e.g., CR11; Hara and Sullivan 2015). The equation of momentum balance has the following form:

$$\overline{U'w'} + \overline{\tilde{U}\tilde{w}} + \overline{p\eta_x} = \tau. \qquad (5)$$

The first term is vertical turbulent flux of momentum, the second is momentum flux generated by wave-produced fluctuations of velocity, and the third term is vertical flux of momentum produced by nonstatic pressure field. The wave-produced flux of momentum $\tau_w = \overline{\tilde{U}\tilde{w}} + \overline{p\eta_x}$ (this kind of stress is absent above flat surface) is a function of wave spectrum and wind profile. This term rapidly decays away from the surface. The sum of all the terms in the left-hand side of (5) should be constant over vertical coordinate z in the bottom boundary sublayer and equal to the external flux of momentum. Terms $\overline{U'w'}$ and $\overline{\tilde{U}\tilde{w}}$ are difficult to separate, but the former attenuates when approaching the surface

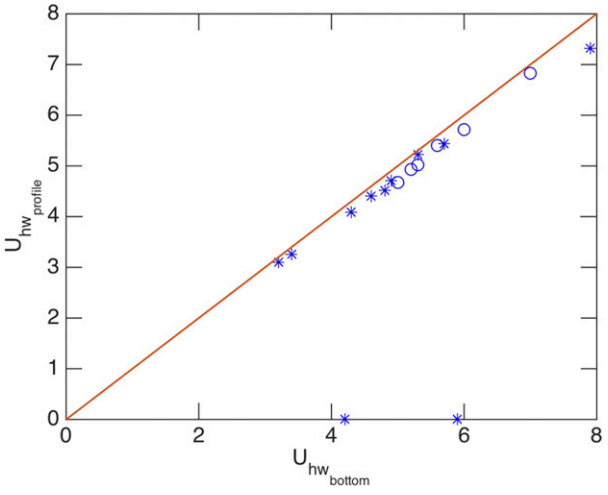

FIG. 2. Measured wind speed at the bottom hot wire (horizontal scale) vs predicted mean wind speed at this hot wire, based on the logarithmic profile (vertical scale). Asterisks indicate the following mode and circles the fixed mode.

and is strictly zero on the surface owing to surface kinematic condition. Note that (5) is obtained in the surface-following coordinate system; hence, $\tilde{w}$ is not Cartesian but a contravariant component of velocity (i.e., it should be measured in the surface-following system). After averaging, the curvilinear coordinate system can be treated as Cartesian. Term $\overline{U'w'}$ in (5) corresponds to a stress produced by velocity shear. As seen, near wavy surfaces this purely turbulent stress should usually be less than the total stress τ.

Such structure of a boundary layer can be modeled with one-dimensional (1D) equations of the WBL. The 1D model of the WBL developed by CR11 was employed in this paper. It is based on evolutionary equations for velocity u, kinetic energy of turbulence e, and rate of its dissipation ε:

$$\frac{\partial u}{\partial t} = \frac{\partial}{\partial z}\left(K\frac{\partial u}{\partial z} + \tau_w\right), \tag{6}$$

$$\frac{\partial e}{\partial t} = \frac{\partial}{\partial z}K_e\frac{\partial e}{\partial z} + P - \varepsilon, \quad \text{and} \tag{7}$$

$$\frac{\partial \varepsilon}{\partial t} = \frac{\partial}{\partial z}K_\varepsilon\frac{\partial \varepsilon}{\partial z} + \frac{\varepsilon}{e}(c_2P - c_4\varepsilon), \tag{8}$$

where $K = c_K e^2/\varepsilon$ is the coefficient of the turbulent viscosity, and the diffusion coefficients K_e and K_ε are proportional to K (i.e., $K_e = K/c_e$ and $K_\varepsilon = K/c_\varepsilon$). In accordance with CR11, coefficients are $c_e = c_\varepsilon = 1$, $c_4 = (c_1 - c_2)\kappa^{-2}c_3^{-1}$, $c_1 = 3.7$, $c_2 = 1.92$, $c_3 = 1.3$. The P is the rate of production of the turbulent kinetic energy:

$$P = \frac{\partial u}{\partial z}\left(K\frac{\partial u}{\partial z} + \tau_w\right). \tag{9}$$

The τ_w is the flux of momentum produced by the wave-induced fluctuations of velocity, stresses, and pressure. According to CR11, τ_w can be calculated by integration of the wave-produced momentum flux (WPMF) over the spectrum:

$$\tau_w = \int_0^{k(\omega_r)} \tau_w^k \exp[-G(\tilde{\omega})kz]\,dk, \tag{10}$$

where $k(\omega_r)$ is the highest wavenumber (corresponding to the highest radian frequency ω_r through the dispersion relationship), $\tilde{\omega} = \omega/\omega_p$ is frequency relative to the peak frequency ω_p. The flux is calculated over a broad range of relative frequencies ω/ω_p and wind forcing $\beta_{-k}\tau_w^k$ (see $\tilde{\Omega}_k$ below). The $G(\tilde{\omega})$ is defined by

$$G = 0.985 + 0.4\tilde{\omega}^{0.81}, \tag{11}$$

and the Fourier components of WPMF on the surface are defined through the following expression:

$$\tau_w^k = kg\beta_{-k}(\tilde{\Omega}_k)S(k), \tag{12}$$

where β_{-k} is determined by (66a) in CR11; $\tilde{\Omega}_k = \omega u(\lambda_k/2)\cos\theta/g$ is the apparent frequency that also characterizes the find forcing; $S(k)\Delta k = 0.5(h_k^2 + h_{-k}^2)$, where $S(k)$ is wavenumber spectrum and h_k and h_{-k} are the respective wave amplitudes. Furthermore, $u(\lambda_k/2)$ is the wind speed at height $z = \lambda_k/2$, where $\lambda_k = 2\pi/k$. Values of $u(\lambda_k/2)$ were calculated using the log-linear interpolation from $u(z)$ profiles. For low-wavenumber modes, height $z = \lambda_k/2$ often exceeds WBL height H_a, and the value of $u(\lambda_k/2)$ was then calculated using the log-linear extrapolation (this is for $\omega < \omega_p$ only).

At the upper boundary $z = 10$ m, the following properties are assigned: wind velocity is U_{10}; rate of production of energy of turbulence P_H is given by

$$P_H = \frac{\upsilon_*^3}{\kappa H_a}, \tag{13}$$

($\upsilon_* = \tau^{1/2}$ is the external friction velocity at $z = H_a$); and the energy of turbulence and the rate of dissipation ε assume the following values:

$$e_H = c_1\upsilon_*^2, \quad \text{and} \tag{14}$$

$$\varepsilon_H = \frac{\upsilon_*^3}{\kappa H_a}. \tag{15}$$

Vertical diffusion of the turbulent energy $K_e(\partial e/\partial z) = 0$ at $z = 0$, as well as at the upper boundary of the domain $z = H_a$. Vertical diffusion of the dissipation rate at $z = 0$ and at $z = H_a$ is, respectively, given by the following:

$$K_\varepsilon\frac{\partial \varepsilon}{\partial z} = -\upsilon_{s0}^4 z_1^{-1}c_3^{-1}, \quad \text{and} \tag{16}$$

$$K_\varepsilon\frac{\partial \varepsilon}{\partial z} = -\upsilon_*^4 H_a^{-1}c_3^{-1}, \tag{17}$$

where $\upsilon_{s0} = \tau_{0t}^{1/2}$ is the local tangential friction velocity defined by the local turbulent tangential stress at the interface τ_{0t}.

An advantage of the 1D model is that it is much simpler than a 2D model. Therefore, the wave spectrum can be extended up to very high wavenumbers. The highest wavenumber is limited by the upper bounds of the dimensionless frequency $\tilde{\Omega} = \pm 50$ in the approximation for function β given in CR11. It was assumed that at the horizontal scales on the order of the resolution limit g/ω_r^2, sea surface can be considered as a smooth surface, so the local roughness parameter z_{0l} can be taken in the form (Monin and Yaglom 1971)

$$z_{0l} = 0.1\nu/\upsilon_{0z}, \tag{18}$$

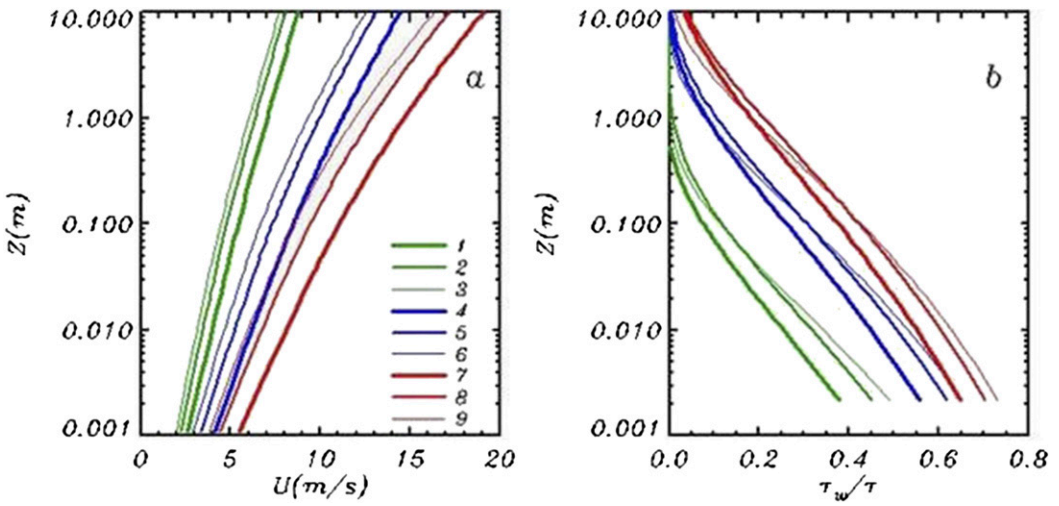

FIG. 3. WBL simulation by means of the CR11 model, for different values of friction velocity u_* and inverse wave age U/c_p: $u_* = 0.3$ for lines 1, 2, and 3; $u_* = 0.6$ for lines 4, 5, and 6; $u_* = 0.9$ for lines 7, 8, and 9; $U/c_p = 0.855$ for lines 1, 4, and 7; $U/c_p = 1.25$ for lines 2, 5, and 8; and $U/c_p = 2.0$ for lines 3, 6, and 9, respectively. (a) Wind velocity profiles for the lower 10 m. (b) Profiles of WPMF τ_w normalized by the upper value of horizontal stress τ.

where $\nu = 0.15 \times 10^{-4}\,\mathrm{m^2\,s^{-1}}$ is the molecular kinematic viscosity, $\upsilon_{0z} = \tau_0^{1/2}$ is the local friction velocity, and τ_0 is the local tangential stress defined by velocity at the water surface u_0. Here we use the drag coefficient $C_l = [k/\ln(\Delta z_1/z_{0l})]^2$, with the thickness of the lowest level Δz_1 equal to $2z_\nu$ ($z_\nu = 60\nu/\upsilon_*$ is the height of the viscous sublayer):

$$\tau_0 = C_l(u_1 - u_0)|u_1 - u_0|, \tag{19}$$

where u_1 is velocity at the lowest level in the air.

Numerical solutions for (6)–(12) are obtained by using the second-order scheme on a stretched grid with stretching coefficient $\gamma = 1.07$ and an explicit time scheme. The explicit scheme requires a very small time step of $\Delta t \sim 10^{-3}$ s estimated through the following relation:

$$\Delta t = 0.25 \min\left[\frac{(\Delta z)^2}{K}\right], \tag{20}$$

but for extensive calculations the semi-implicit scheme is more appropriate. For the stationary solution, the condition $\tau_z = K\partial u/\partial z + \tau_w = \tau$ must be satisfied over the entire WBL. The criterion for reaching the stationary solution is taken in the following form:

$$[\max(\tau_z) - \min(\tau_z)]/\tau < 0.01. \tag{21}$$

In CR11, the problem of mutual adjustment of the wave spectrum and the wind was solved. In the current work, the wind velocity U_{10} and wave spectrum were fixed, and therefore the vertical profile of wind and components of the stress $K\partial u/\partial z$ and τ_w were calculated.

The stationary dynamic structure of the WBL is described by x-momentum balance [(5)] as

$$\frac{\partial}{\partial z}\left(K\frac{\partial u}{\partial z} + \tau_w\right) = 0 \tag{22}$$

and is shown in Fig. 3. Each group of data here (green, blue, and red) refers to a different friction velocity from the set of $u_* = (0.3,\ 0.6,\ 0.9)\ \mathrm{m\,s^{-1}}$, and a line within each group corresponds to a different inverse wave age $U_{10}/c_p = (0.855, 1.25, 2)$ from right to left (c_p is the phase speed of peak waves).

Figure 3a shows respective wind profiles, disturbed by waves through WPMF, in semilogarithmic scale for groups color coded for different friction velocities. As seen, with an increase of inverse wave age within each group, the slope of logarithmic wind profile increases and wind speed, respectively, decreases. Apart from light-wind conditions, the wind speed at small heights near the surface is noticeably larger than what could be inferred from an "undisturbed" logarithmic boundary layer near the standard 10-m height. Hence, if measurements are done very near the surface (e.g., by buoys in presence of large waves) and then extrapolated up to 10 m, results will be biased high. Depending on the buoy-measurement height, wind speed, and sea state, extrapolations from one height to another can lead to very substantial deviations. The wave heights, predicted on the basis of such winds, will be biased even stronger because dependence of waves on wind is nonlinear (quadratic in simple cases of wave development).

The total flux [(5)] should be constant through the boundary layer, even though the relative contributions of the different dynamic terms change toward the surface, in case of the wavy air–sea interface. This makes it a convenient property for comparisons as its magnitude should not depend on the elevation z at which it is measured. In Fig. 3b, vertical profiles of wave-produced momentum flux τ_w, normalized by such an upper (undisturbed) value of vertical momentum flux τ, are shown. The WPMF increases with wind speed and wind forcing (inverse wave age). It is apparent that for every wind speed and at each sea state, contribution of τ_w into the total stress grows toward the water surface, and hence turbulent flux $\overline{U'w'}$ in (5), if estimated close to the surface ($z = 0$), is significantly less than the total flux at 10-m height.

4. Summary

In this paper, measurements of winds and turbulent stresses very near the surface of ocean waves are conducted and compared with measurements within the constant-flux layer away from the surface. The turbulent stress toward the surface is reduced dramatically, some 7 times in the presented conditions and experimental setup, whereas the mean wind speed is increased by some 5% compared to extrapolations based on the logarithmic profile. The behavior is then simulated by means of a three-dimensional WBL model coupled with nonlinear waves and is confirmed. The wave-induced vertical flux of momentum produced by the nonstatic pressure field very near the surface is responsible for reduction of the apparent turbulent stress.

The practical significance of such observations is large, for example, for measurements conducted within the wave boundary layer by buoys. If such buoy wind speeds are extrapolated away from the surface by means of logarithmic profiles, to the 10-m standard height or above, the actual values of wind speeds may be overestimated, which will then result in even greater relative overestimation of wave heights once the wave-forecast models are forced to assimilate such winds. If the buoys are used to measure turbulent stresses directly, then, depending on the height of the anemometer mast on the buoy, such stresses can be essentially underestimated.

Acknowledgments. AVB acknowledges ARC Discovery Grant DP170101328 and DISI Australia-China Centre through Grant ACSRF48199, and Woodside Energy, Ltd., through an industry grant. The results of section 3 were obtained in the framework of the state assignment of FASO Russia (Theme 0149-2018-0014).

REFERENCES

Babanin, A. V., 2009: Breaking of ocean surface waves. *Acta Phys. Slovaca*, **59**, 305–535, https://doi.org/10.2478/v10155-010-0097-5.

——, and V. K. Makin, 2008: Effects of wind trend and gustiness on the sea drag: Lake George study. *J. Geophys. Res.*, **113**, C02015, https://doi.org/10.1029/2007JC004233.

——, and J. McConochie, 2013: Wind measurements near the surface of waves. *Proc. ASME 2013 32nd Int. Conf. on Ocean, Offshore and Arctic Engineering*, Nantes, France, American Society of Mechanical Engineers, OMAE2013-10146.

——, I. R. Young, and H. Mirfenderesk, 2005: Field and laboratory measurements of wave-bottom interaction. *Proc. 17th Australasian Coastal and Ocean Engineering Conf./10th Australasian Port and Harbour Engineering Conf.*, Adelaide, South Australia, Australia, Institution of Engineers, 293–298.

——, M. L. Banner, I. R. Young, and M. A. Donelan, 2007: Wave-follower measurements of the wind-input spectral function. Part III: Parameterization of the wind input enhancement due to wave breaking. *J. Phys. Oceanogr.*, **37**, 2764–2775, https://doi.org/10.1175/2007JPO3757.1.

——, G. G. Wake, and J. McConochie, 2016: Field observation site for air-sea interactions in tropical cyclones. *Proc. ASME 2016 35th Int. Conf. on Ocean, Offshore and Arctic Engineering*, Busan, South Korea, American Society of Mechanical Engineers, OMAE2016-54570.

Chalikov, D., and M. Belevich, 1993: One-dimensional theory of the wave boundary layer. *Bound.-Layer Meteor.*, **63**, 65–96, https://doi.org/10.1007/BF00705377.

——, and S. Rainchik, 2011: Coupled numerical modelling of wind and waves and the theory of wave boundary layer. *Bound.-Layer Meteor.*, **138**, 1–41, https://doi.org/10.1007/s10546-010-9543-7.

Donelan, M. A., 1999: Wind-induced growth and attenuation of laboratory waves. *Wind-over-Wave Couplings: Perspective and Prospects.* S. G. Sajadi, N. H. Thomas, and J. C. R. Hunt, Eds., Clarendon Press, 183–194.

——, A. V. Babanin, I. R. Young, M. L. Banner, and C. McCormick, 2005: Wave-follower field measurements of the wind-input spectral function. Part I: Measurements and calibrations. *J. Atmos. Oceanic Technol.*, **22**, 799–813, https://doi.org/10.1175/JTECH1725.1.

——, ——, ——, and ——, 2006: Wave follower measurements of the wind input spectral function. Part II: Parameterization of the wind input. *J. Phys. Oceanogr.*, **36**, 1672–1688, https://doi.org/10.1175/JPO2933.1.

——, M. Curcic, S. S. Chen, and A.-K. Magnusson, 2012: Modeling waves and wind stress. *J. Geophys. Res.*, **117**, C00J23, https://doi.org/10.1029/2011JC007787.

Elliott, J. A., 1972: Instrumentation for measuring static pressure fluctuations within the atmospheric boundary layer. *Bound.-Layer Meteor.*, **2**, 476–495, https://doi.org/10.1007/BF00821550.

Hara, T., and P. P. Sullivan, 2015: Wave boundary layer turbulence over surface waves in a strongly forced condition. *J. Phys. Oceanogr.*, **45**, 868–883, https://doi.org/10.1175/JPO-D-14-0116.1.

Hasselmann, K., 1962: On the non-linear energy transfer in a gravity-wave spectrum: Part 1. General theory. *J. Fluid Mech.*, **12**, 481–500, https://doi.org/10.1017/S0022112062000373.

Howden, S., D. Gilhousen, N. Guinasso, J. Walpert, M. Sturgeon, and L. Bender, 2008: Hurricane Katrina winds measured by a buoy-mounted sonic anemometer. *J. Atmos. Oceanic Technol.*, **25**, 607–616, https://doi.org/10.1175/2007JTECHO518.1.

Iafrati, A., A. V. Babanin, and M. Onorato, 2013: Modulational instability, wave breaking and formation of large scale dipoles. *Phys. Rev. Lett.*, **110**, 184504, https://doi.org/10.1103/PhysRevLett.110.184504.

——, ——, and ——, 2014: Modelling of ocean–atmosphere interaction phenomena during the breaking of modulated wave trains. *J. Comput. Phys.*, **271**, 151–171, https://doi.org/10.1016/j.jcp.2013.12.045.

Kitaigorodskii, S. A., 1970: *Physics of Atmosphere and Ocean Interaction* (in Russian). Gidrometeoizdat, 284 pp.

Komen, G. I., L. Cavaleri, M. Donelan, K. Hasselmann, S. Hasselmann, and P. A. E. M. Janssen, 1994: *Dynamics and Modelling of Ocean Waves.* Cambridge University Press, 554 pp.

Kudryavtsev, V. N., V. K. Makin, and J. F. Meinrik, 2001: Simplified model of the air flow above the waves. *Bound.-Layer Meteor.*, **98**, 155–171, https://doi.org/10.1023/A:1018719917275.

Landau, L. D., and E. M. Lifshitz, 1987: *Fluid Mechanics.* Pergamon Press, 539 pp.

Monin, A. S., and A. M. Obukhov, 1954: Basic laws of turbulent mixing in the atmosphere near the ground (in Russian). *Tr. Geofiz. Inst., Akad. Nauk SSSR*, **24**, 163–187.

——, and A. M. Yaglom, 1971: *Statistical Fluid Mechanics: Mechanics of Turbulence.* Vol. 1. MIT Press, 769 pp.

Pierson, W. J., Jr., and L. Moskowitz, 1964: A proposed spectral form for fully developed wind seas based on the similarity theory of S. A. Kitaigorodskii. *J. Geophys. Res.*, **69**, 5181–5190, https://doi.org/10.1029/JZ069i024p05181.

Pond, S., 1968: Some effects of buoy motion on measurements of wind speed and stress. *J. Geophys. Res.*, **73**, 507–512, https://doi.org/10.1029/JB073i002p00507.

Skey, S. G. P., K. Berger-North, and V. R. Swail, 1998: Measurement of winds and waves from a NOMAD buoy in high seastates. Preprints, *5th Int. Workshop on Wave Hindcasting and Forecasting*, Melbourne, FL, Environment Canada, 163–173, http://www.waveworkshop.org/5thWaves/5thWaves_Complete.pdf.

Taylor, P. K., E. Dunlap, F. W. Dobson, R. J. Anderson, and V. R. Swail, 2002: On the accuracy of wind and wave measurements from buoys. Data Buoy Cooperation Panel Tech. Doc. 21, 15 pp., www.jcommops.org/dbcp/doc/DBCP-21/DOCS_DBCP21/27%20Taylor.doc.

Young, I. R., M. L. Banner, M. A. Donelan, A. V. Babanin, W. K. Melville, F. Veron, and C. McCormick, 2005: An integrated system for the study of wind wave source terms in finite depth water. *J. Atmos. Oceanic Technol.*, **22**, 814–828, https://doi.org/10.1175/JTECH1726.1.